Geophysical Research Letters

RESEARCH LETTER
10.1029/2023GL104719

Arctic Spring Systems Driven by Permafrost Aggradation

Mikkel Toft Hornum[1,2], Victor Bense[3], Martine van der Ploeg[3], Aart Kroon[1], and Ylva Sjöberg[1]

[1]Department of Geosciences and Natural Resource Management, and Center for Permafrost, University of Copenhagen, Copenhagen, Denmark, [2]Department of Arctic Geology, The University Centre in Svalbard, Longyearbyen, Norway, [3]Department of Environmental Sciences, Wageningen University, Wageningen, the Netherlands

Key Points:

- Hydraulic pressure generation from millennial-scale permafrost aggradation is investigated as a new mechanism for driving groundwater flow
- Freezing pressure induced at the base of aggrading permafrost can drive Arctic spring systems for millennia
- This mechanism deserves attention in areas of recent glacio-isostatic uplift and glacial retreat

Correspondence to:
M. T. Hornum,
mth@ign.ku.dk

Citation:
Hornum, M. T., Bense, V., van der Ploeg, M., Kroon, A., & Sjöberg, Y. (2023). Arctic spring systems driven by permafrost aggradation. *Geophysical Research Letters*, *50*, e2023GL104719. https://doi.org/10.1029/2023GL104719

Received 1 JUN 2023
Accepted 9 AUG 2023

Author Contributions:
Conceptualization: Mikkel Toft Hornum, Victor Bense, Martine van der Ploeg, Ylva Sjöberg
Formal analysis: Mikkel Toft Hornum, Victor Bense, Ylva Sjöberg
Funding acquisition: Ylva Sjöberg
Investigation: Mikkel Toft Hornum
Methodology: Mikkel Toft Hornum, Victor Bense, Ylva Sjöberg
Software: Mikkel Toft Hornum, Victor Bense
Supervision: Victor Bense, Aart Kroon, Ylva Sjöberg
Visualization: Mikkel Toft Hornum, Ylva Sjöberg
Writing – original draft: Mikkel Toft Hornum, Ylva Sjöberg
Writing – review & editing: Mikkel Toft Hornum, Victor Bense, Martine van der Ploeg, Aart Kroon, Ylva Sjöberg

Abstract Groundwater springs in permafrost regions provide pathways for solutes and dissolved gases to escape from sub-permafrost groundwater systems, which otherwise are completely isolated from the surface environment and atmosphere. Yet, fundamental questions as to the mechanisms driving groundwater flow to the surface remain unsolved. In this study, basal permafrost aggradation is explored as a mechanism for generating groundwater flow and driving groundwater spring systems. We employ process-based numerical modeling to test the hypothesis of permafrost-aggradation-driven spring systems in a range of environmental settings. The model results show that permafrost aggradation can generate spring flow on a multi-millennial timescale and with discharge rates up to a couple of liters per second. Permafrost aggradation deserves attention as a groundwater flow driving mechanism in areas of recent glacio-isostatic uplift and glacial retreat.

Plain Language Summary In the High Arctic, the subsurface is frozen in a state called permafrost. Since fluids cannot flow through ice, surface water only flows close to the surface, while groundwater below the permafrost is trapped—sometimes along with large amounts of greenhouse gases. In some permafrost locations, groundwater springs allow groundwater to reach the surface and atmosphere from the deep subsurface. Unlike non-permafrost regions, these locations often lack routes for surface water to flow beneath the permafrost, which means that the spring outflow is not balanced by incoming water. In this study, we investigate the idea that when permafrost grows deeper, the expansion of groundwater as it freezes creates enough pressure to cause the spring outflow. We use a computer model to simulate this process, and our results show that permafrost growth can generate spring outflow for millennia, reaching a flow rate of a few liters per second. This new understanding is crucial for predicting how greenhouse gas emissions from groundwater springs in permafrost will respond to climate change. It is also relevant for the long-term deposition of hazardous materials, such as nuclear waste, as it provides a mechanism for contaminants to spread from the deep subsurface to surface systems.

1. Introduction

Several mechanisms can lead to the movement of groundwater. Topography-driven groundwater flow is generally dominant (Tóth, 1970), while other mechanisms may be locally important. Other, well-established mechanisms include density-driven, compaction-driven, and osmosis-driven groundwater flow (Kooi et al., 2003; Neuzil, 1995). In this work, we simulate a hydrogeological system wherein hydraulic gradients are produced by millennial-scale permafrost aggradation. This permafrost-aggradation-driven groundwater flow may be essential to understand millennial-scale groundwater movement in the Northern Hemisphere (NH) where the extent of permafrost changes with >30 mio. km^2 (~30% percent of current NH land masses) between glacial and interglacial periods (Lindgren et al., 2016; Saito et al., 2022).

In High Arctic regions, groundwater flow is restricted by continuous permafrost that effectively separates deep sub-permafrost groundwater from the surface and atmosphere. Groundwater flow and solute transport between the deep groundwater and surface systems are therefore limited to unfrozen zones (i.e., taliks) that locally perforate the frozen ground. Such taliks can result from thermal insulation at the surface provided by larger water bodies and glaciers (e.g., Johansson et al., 2015; Liestøl, 1977), or from below springs where advective heat transfer associated with the upwelling of sub-permafrost groundwater locally prevents the ground from freezing (Andersen et al., 2002). As for such spring systems, the mechanism responsible for sustaining the flow of deep groundwater to the surface remains elusive (Scheidegger et al., 2012). Earlier studies have proposed that recharge from meltwater below warm-based glacial ice can provide the required hydraulic pressure to sustain spring flow

(Haldorsen et al., 1996; Liestøl, 1977; Scheidegger et al., 2012). However, some springs are located in areas where warm-based glaciers or alternative recharge pathways are lacking (Ballantyne, 2018; Grasby et al., 2014). Hornum et al. (2020) therefore proposed an alternative explanation wherein freezing pressure resulting from basal permafrost aggradation drives spring outflow.

Previous numerical modeling experiments have shown that hydraulic heads produced at the base of ice sheets can maintain spring outflow for millennia, even when permafrost is aggrading (disregarding freezing expansion, Scheidegger et al., 2012; Scheidegger & Bense, 2014). Hornum et al. (2020) simulated the Holocene hydraulic pressure production from permafrost aggradation in an uplifted valley on Svalbard with a 1D heat transfer model and used a 3D groundwater model to show that these hydraulic pressures may explain observed spring discharge rates.

The hypothesis that Hornum et al. (2020) present gives rise to questions about the potential magnitude and timescale of spring systems maintained by basal permafrost aggradation. Would this mechanism explain the continued outflow observed from springs in the absence of ice sheets or warm-based glaciers? To investigate, we employ a process-based modeling approach aligning with benchmark cryohydrological modeling tools (Grenier et al., 2018, and references therein). We consider the bottom of sediment-filled, low-lying Arctic valleys to be the most likely locations of spring systems wherein hydraulic heads are produced by aggrading permafrost pressure, and we therefore focus on these valleys. Here, the permafrost is typically of Holocene age, as it developed after and due to ice sheet retreat or land emergence and, in some regions, only after the Holocene thermal maximum (Greenland: Garcia-Oteyza et al., 2022; Scholz & Grottenthaler, 1988. Svalbard: Humlum et al., 2005; Ingólfsson & Landvik, 2013. Canadian Arctic: England, 1992). We also evaluate spring pore water velocity changes during talik freeze-up and discuss the implications for the possible transfer of solutes stored beneath permafrost to the surface.

1.1. Conceptual Model for Permafrost-Aggradation-Driven Spring Formation

Groundwater systems developing with permafrost growth result in a particular hydrogeological setting wherein hydraulic pressures are still being maintained when obvious recharge sources are seemingly often lacking (Grasby et al., 2014). At the aggrading freezing front, pore water expands in its transition to ice and causes a net loss in pore space which can drive groundwater flow, analogous to compaction-driven groundwater flow in active sedimentary basins (e.g., Kooi, 1999). Ice-cored hills (i.e., pingos) which form in hydrologically closed systems within the bottom of drained lakes in the High Arctic constitute a manifestation of this process (Mackay, 1998). Our conceptual model for spring systems maintained by basal permafrost aggradation is illustrated in Figure 1.

The starting point of our simulations ($t = 0$) is a permafrost-free landscape where the subsurface is in thermal equilibrium with a temperature exceeding 0°C. This initial state represents subglacial, submarine (Figure 1a1), or temperate climate conditions (Figure 1a2). Then, the landscape gets exposed to cold atmospheric temperatures due to glacial retreat, marine regression, or climate cooling and permafrost starts to form from the ground surface downwards (Figure 1b). Initially, microtopography causes a distribution of frozen ground and taliks controlled by the variability in snow, water, and vegetation (Sjöberg et al., 2015). When permafrost thickness exceeds a couple of meters, the vertical pressure due to the weight of the overlying sediments restricts excess ice formation and ground heave (French & Shur, 2010). Instead, freezing expansion causes a net pore space loss, which produces hydraulic overpressures at the migrating freezing front (Figure 1c). The increased hydraulic head gradients drive groundwater flow toward the surface through taliks. Advective heat transfer from groundwater flow keeps these taliks permafrost-free. Permafrost-aggradation-driven hydraulic pressure production ceases when ground temperatures have equilibrated to the colder ground surface condition and the geothermal heat flux (Figure 1d), but a dynamic storage effect may keep the groundwater system pressurized for a much longer period. The sub-permafrost groundwater system loses its connection to the surface if no-flow conditions prevail, unless salinity prevents the talik from freezing.

2. Numerical Modeling

We employ a modeling approach wherein processes of groundwater flow and heat transport are fully coupled (Grenier et al., 2018, and references therein). Current examples of modeling tools applied in cryohydrogeological research are numerous (Lamontagne-Hallé et al., 2020). We here simulate with FlexPDE, a finite element

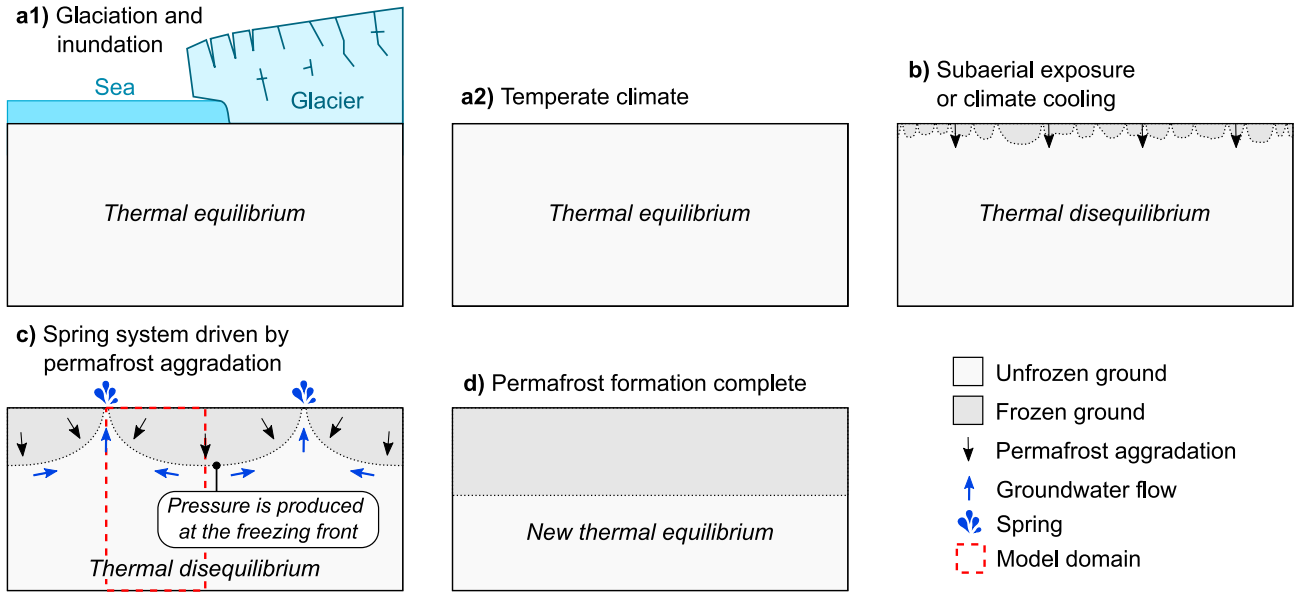

Figure 1. Conceptual model for permafrost-aggradation-driven spring formation. Following permafrost-free conditions during glaciation, sea inundation (a1), or temperate climate (a2), surface temperature drops below 0°C and permafrost starts to form (b). (c) Freezing pressure at the freezing front drives groundwater to the surface through taliks kept open by advective heat transport. (d) If surface temperatures remain constant, the ground eventually reaches a thermal equilibrium and no-flow conditions prevail in the absence of other drivers. The domain for the numerical modeling experiments is outlined in (c) but applies to all panels.

builder and partial differential equations solver (PDE Solutions Inc., 2021), which has been used in similar modeling studies before (Bense et al., 2009; de Bruin et al., 2021; Guimond et al., 2021, 2022; Mohammed et al., 2021, 2022; Scheidegger et al., 2012).

2.1. Governing Equations

The model assumes fully saturated conditions throughout the domain. Salinity-dependent and temperature-dependent variations of material properties are not accounted for here, because they are assumed negligible within the near-surface temperature range (Farouki, 1981).

Groundwater flow was calculated from the transient hydraulic head (h [m]) field as follows:

$$(\beta n \rho_w F_w g)\frac{\partial h}{\partial t} = \nabla \cdot [K_a \nabla h] - n\left(\frac{\rho_w}{\rho_{ice}} - 1\right)\frac{\partial F_w}{\partial t} \quad (1)$$

where β is the matrix compressibility [m s^2 kg^{-1}], n is porosity [-], ρ_w and ρ_{ice} are the densities of water and ice [kg m^{-3}], respectively, F_w is the fraction of water in the pore space [-], g is the gravitational acceleration [m s^{-2}], t is time [s], and K_a is the effective hydraulic conductivity [m s^{-1}]. Our fixed parameter values are listed in Table 1. The second term on the right-hand side of Equation 1 is a source term accounting for pressure effects from freeze and thaw (Grenier et al., 2018). Freezing results in 9% loss of pore space under freshwater conditions.

An advection-diffusion-equation was used to calculate subsurface temperature distributions:

$$C_b \frac{\partial T}{\partial t} = \nabla[\kappa_b \nabla T] - C_b \vec{q} \nabla T - Ln\rho_{ice}\frac{\partial F_{ice}}{\partial t} \quad (2)$$

where C_b is the volumetric heat capacity [J K^{-1} m^{-3}] of the bulk sediment, T is temperature [°C], κ_b is the thermal conductivity [W m^{-1} K^{-1}], C_w is the volumetric heat capacity of water, $\vec{q}$ is the specific groundwater discharge [m

Table 1
Fixed Parameters Values Used in All Model Scenarios

Parameter	Symbol	Value
Thermal conductivity of water	κ_w	0.6 W m^{-1} K^{-1}
Thermal conductivity of ice	κ_{ice}	2.14 W m^{-1} K^{-1}
Thermal conductivity of solids[a]	κ_s	3.5 W m^{-1} K^{-1}
Vol. heat capacity of water	C_w	4,182•10^3 J m^{-3} K^{-1}
Vol. heat capacity of ice	C_{ice}	1,895•10^3 J m^{-3} K^{-1}
Vol. heat capacity of solids	C_s	2,213•10^3 J m^{-3} K^{-1}
Density of water	ρ_w	1,000 kg m^{-3}
Density of ice	ρ_{ice}	920 kg m^{-3}
Latent heat of fusion	L	3.34 J kg^{-1}
Geothermal heat flux	q_T	0.05 W m^{-2}
Residual water fraction	F_{res}	0.05
Gravitational acceleration	g	9.81 m s^{-2}

[a]Grenier et al. (2013). Other values are from Grenier et al. (2018).

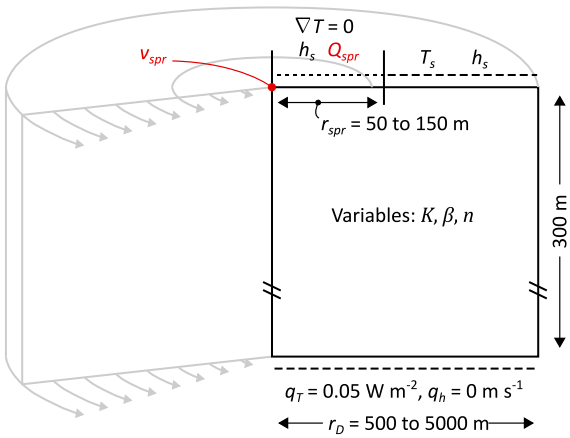

Figure 2. Model domain with boundary conditions, variables, and evaluated output parameters (in red). Outside the spring zone, T_s decreases linearly from 0°C to −4°C during the first 200 or 3,000 years. At the spring zone, T_{spr} equals the temperature of the discharging groundwater (i.e., $\nabla T = 0$). A constant heat flux, q_T, is applied at the base. A hydraulic head of $h_s = 0$ m above ground level is applied at the top, the base is closed for groundwater flow, and the sides are also closed for heat flow. Spring discharge, Q_{spr} [m^3 s^{-1}], is evaluated over the entire spring zone, while the spring pore water velocity, $v_{spr} = q_h(nf_w)^{-1}$ [m s^{-1}], is evaluated at the center.

s^{-1}], L is the latent heat of fusion [J kg^{-1}], and F_{ice} is the fraction of ice in the pore space [-]. On the right-hand side of Equation 2, the first term describes conductive heat transfer, the second term describes advective heat transfer by groundwater flow, and the third term describes latent heat fluxes from freezing and thawing.

For temperatures above 0°C, F_w was 1, while for subzero temperatures, we used a smoothed step function to describe F_w (as done by McKenzie et al., 2007; Mottaghy & Rath, 2006), which had a freezing range of 2°C. The residual water fraction remaining in the pore space at temperatures below the freezing range, F_{res} was 0.05. The fraction of ice occupying the pore space was defined conversely as $F_{ice} = 1 - F_w$. With the assumption of fully saturated conditions, the total fractions of solids, water and ice are given as $f_s = 1n$, $f_w = nF_w$, and $f_{ice} = nF_{ice}$, respectively. Effective thermal properties were defined using these fractions; C_b as a geometric mean (e.g., Grenier et al., 2018), and κ_b as a weighted volumetric square-root mean (e.g., Mottaghy & Rath, 2006).

Ice in the pore space reduces the hydraulic conductivity for temperatures lower than T_L. As done by Scheidegger et al. (2012), we calculated the effective hydraulic conductivity K_a as proportional to the unfrozen hydraulic conductivity (K) and a permeability reduction parameter derived from experimental data presented by Kleinberg and Griffin (2005):

$$K_a = K \frac{F_w^{3.5}}{\left(1 + (1 - F_w)^{0.5}\right)^2} \quad (3)$$

2.2. Modeling Approach

To investigate the proposed mechanism (Figure 1), we simulate the formation and freeze-up of a single talik-spring system. The model domain was set up in axis-symmetrical geometry as a radial cross-section of a cylinder with the spring zone located at the center of the upper surface at radii less than 50–150 m (Figure 2). The domain was 300 m thick for all scenarios, while the lateral extent (i.e., radius) was either 1,000, 2,500 or 5,000 m to represent spring systems located in different valley and catchment sizes.

Hydrogeological and thermal parameters were assumed homogeneous and isotropic and selected to represent a realistic range of valley settings (Tables 1 and 2). We assumed that a typical Arctic valley geometry is represented by a symmetrical model setup with flat topography.

The domain sides and bottom were closed for groundwater flow and the upper boundary was assigned with a hydraulic head at ground surface elevation (0 m). At the perimeter side, a no-flow condition represents a hydraulic divide toward a neighboring spring or very low-permeable rocks encountered toward the side of a valley. There are no external pressure sources and fluid flow is assumed driven exclusively by pressure produced by freezing of the saturated pore space (last term in Equation 1).

The model sides were closed for heat transfer, while a constant heat flux was assigned to the bottom to represent geothermal heat flow (Table 2). At the spring zone, a zero temperature gradient was applied to the upper

Table 2
Variable Values Used in Model Scenarios

Parameter	Low value	Base case value	High value
Spring zone radius, r_{spr}	50 m	100 m	150 m
Domain radius, r_D	1,000 m	2,500 m	5,000 m
Porosity, n	0.3	0.4	0.5
Hydraulic conductivity of unfrozen sediment, K	$1.6{\cdot}10^{-8}$ m s^{-1}	$1.6{\cdot}10^{-7}$ m s^{-1}	$1.6{\cdot}10^{-6}$ m s^{-1}
Matrix compressibility, β	10^{-9} m s^2 kg^{-1}	10^{-8} m s^2 kg^{-1}	10^{-7} m s^2 kg^{-1}

boundary, allowing heat to exit the domain solely through advective transport with spring discharge. Along the remaining upper boundary, permafrost formation was driven by a decreasing time-varying surface temperature, T_s.

2.3. Scenarios

Initial ground temperatures were calculated at steady-state given a surface temperature of state 0°C and the heat flux specified at the model base. Hence, pore ice was not present at the beginning of all simulations. All scenarios were run for 10 Kyr (Kyr = 10^3 years) of simulation time.

2.3.1. Temperature Curve

One set of scenarios considers subaerial exposure due to marine or glacial regression, which has been common in the Arctic throughout the Holocene (Pirazzoli & Pluet, 1991). Subaerial exposure is represented by a relatively sudden linear decrease of T_s from 0°C to −4°C in the first 200 years of simulation time (starting point depicted by Figure 1a1). In a second set of scenarios, T_s instead decreased during the first 3 Kyr of simulation time (Figure 1a2), which mimics typical climate cooling following the Holocene thermal maximum on Svalbard (Mangerud & Svendsen, 2017) and in Arctic Canada and Greenland (Briner et al., 2016).

2.3.2. Controls on Model Behavior

In the model scenarios included here, five parameters were included as variables to represent spring systems in a range of settings: spring zone radius, domain radius, porosity, hydraulic conductivity, and matrix compressibility (Table 2). Each of these variables had a base case value in a first set of model runs, while a second set of model runs simulated scenarios with low and high values. Spring zone and domain radii were included as variables to represent spring systems across a spatial scale. Other parameters were included if changing them—within a range representing possible valley settings (hydrogeological, thermal, geographical)—had a significant impact on the simulated duration or rate of spring discharge. As such, the geothermal heat flux and thermal conductivity of solids were, for example, not included as these parameters only had a marginal effect on the evaluated simulation results.

3. Results

Simulated rates of spring discharge, Q_{spr} [$m^3\ s^{-1}$], and pore water velocity, $v_{spr} = q_h(nf_w)^{-1}$ [$m\ s^{-1}$], for the scenarios with varying domain radii are shown in Figures 3a and 3b. Peak Q_{spr} and duration of spring discharge, $\Delta t_{Q_{spr}}$, for all scenarios are summarized in Figure 4. We defined $\Delta t_{Q_{spr}}$ as the duration of the period where $Q_{spr} \geq 10^{-2}$ L s^{-1}.

For all scenarios, Q_{spr} peaks within the first half of the discharge period. For most scenarios, the peak value occurs within 100 years following the end of the surface temperature drop. The scenarios with 1,000 m domain radius and climate cooling (Figure 3a) and 5,000 m domain radius and exposure (Figure 3b) exemplify the exceptions—that is, respectively, scenarios with low and high Q_{spr}. For these, respectively, Q_{spr} peaks before or up to 500 years after the end of the temperature drop.

The v_{spr} versus time curves have a less uniform pattern by often showing two kinks (exemplified with arrows on Figure 3a). If present, the first kink coincides with the maximum rate of Q_{spr}, while the second kink coincides with talik closure: v_{spr} increases to its maximum value when a completely unfrozen conduit is no longer present below the spring zone (exemplified in Figures 3a and 3c).

With increasing domain radius, spring zone radius, porosity, and hydraulic conductivity, but with decreasing matrix compressibility, the talik is kept open for a longer period allowing for a correspondingly longer $\Delta t_{Q_{spr}}$ during and after permafrost growth (Figure 4b). The maximum rate of Q_{spr} is correlated with the five variables in the same way, although porosity changes have a neglectable effect (Figure 4a).

For most scenarios, $\Delta t_{Q_{spr}}$ varies from 3 to 7 Kyr with the only exceptions being the small and large spring zone radius cases, respectively resulting in $\Delta t_{Q_{spr}} \approx 1$ kyr and $\Delta t_{Q_{spr}} > 7.5$ kyr (Figure 4b). The geometrical parameter variables have the greatest impact on $\Delta t_{Q_{spr}}$ with spring zone radius being more important than domain radius, r_D (Figure 4b). For the scenarios with climate cooling and varying domain radius, permafrost aggradation generates enough artesian pressure for spring discharge from approximate 1–5 Kyr after the simulation start ($t = 0$)

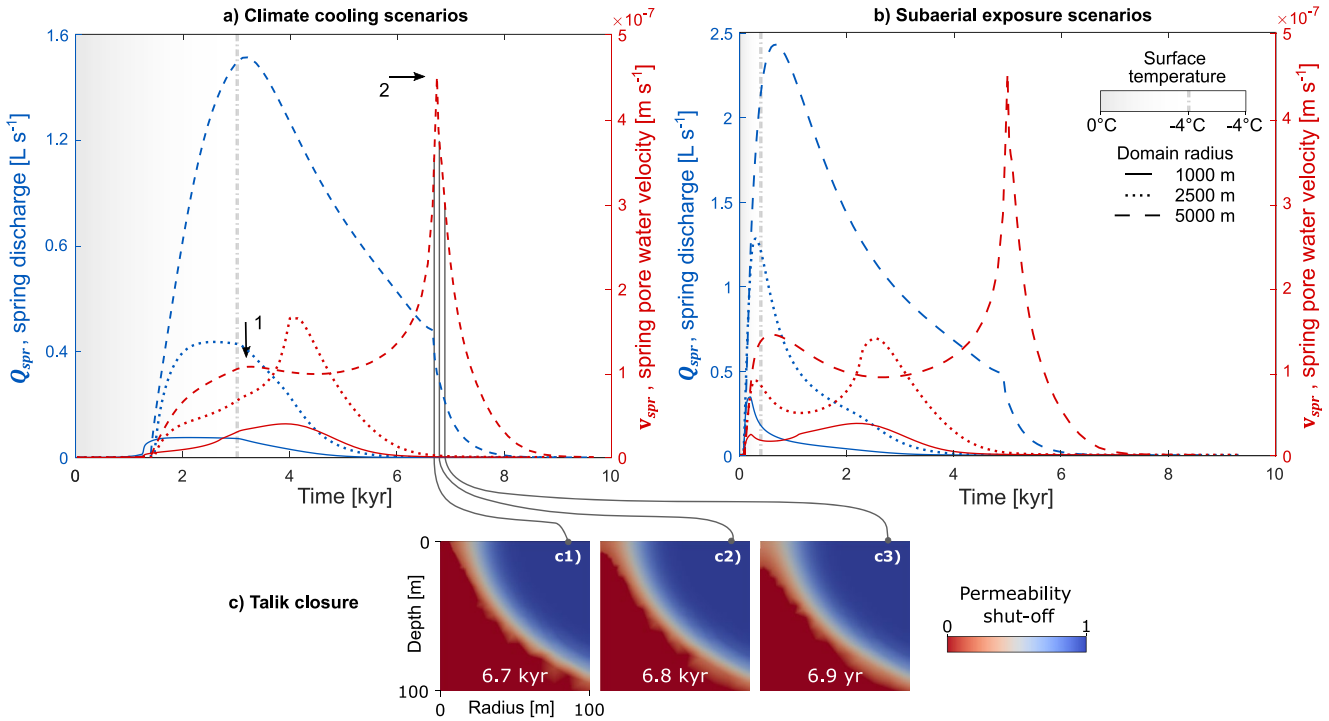

Figure 3. Simulated rates of spring discharge, Q_{spr} [L s^{-1}], and spring pore water velocity, v_{spr} [m s^{-1}], for scenarios with different domain radii. Illustrated by the gray-to-white color scale, ground temperature changes are driven by a linear decrease of the ground surface temperature from 0°C to −4°C during the first 3 (a) or 0.2 Kyr (b). Please note difference in scale of left *y*-axis between panels (a) and (b). (c) Snapshots of talik closure from the climate cooling scenario with large domain radius (r_D = 5,000 m).

with small domain radius (r_D = 1,000 m), 1–6 Kyr with medium radius (r_D = 2,500 m), and 1–8 Kyr with large radius (r_D = 5,000 m). Q_{spr} peaks at 0.08, 0.44, and 1.51 L s^{-1} respectively for the small, medium, and large domain radius cases. For the same three domain radii but with subaerial exposure (Figure 3b), spring discharge is generated for similar lengths of time, but starts earlier at $t \approx 50$ years, and peak rates of Q_{spr} are 0.34, 1.28, and 2.43 L s^{-1}, respectively.

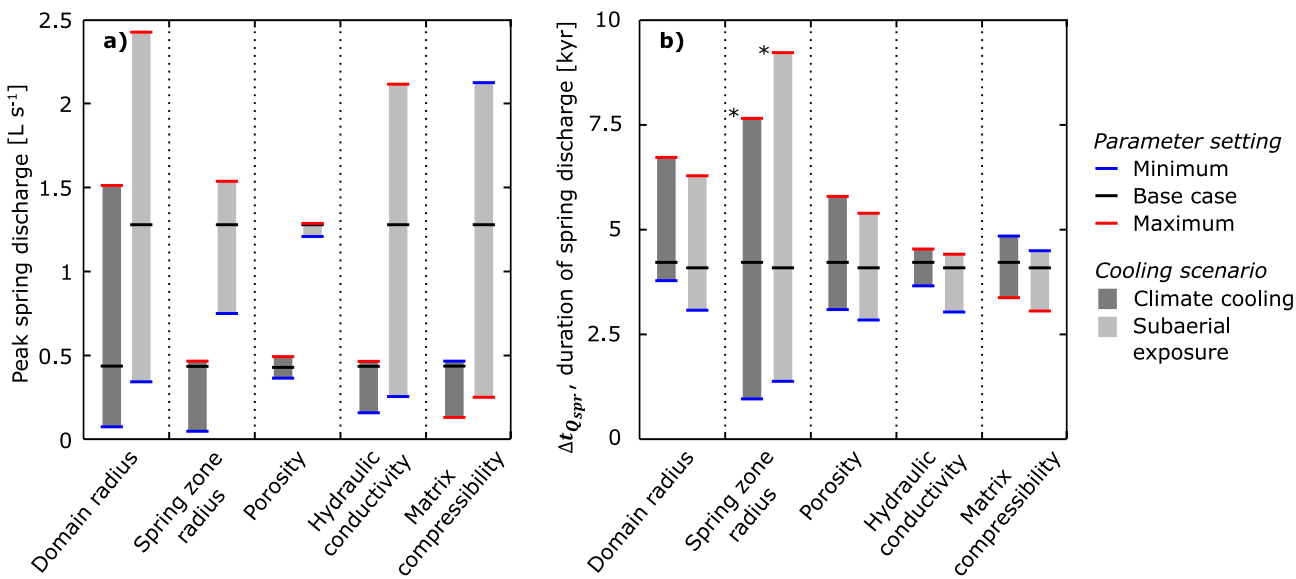

Figure 4. Simulated peak spring discharge (a) and duration of spring discharge, $\Delta t_{Q_{spr}}$, (b) with the different cases for domain and spring zone radii, porosity, hydraulic conductivity, and matrix compressibility (Table 2). Dark and light gray ranges indicate climate cooling and exposure scenarios, respectively. *Spring discharge did not cease within the simulation time (t = 10 Kyr) for the scenarios with maximum spring zone radius (r_{spr} = 150 m).

Simulated evolution of Q_{spr} and v_{spr} is delayed for the climate cooling scenarios (Figure 3a) relative to the subaerial exposure scenarios (Figure 3b). The delay is the only clear influence on the maximum v_{spr}, while rates of v_{spr} at the end of the surface temperature drop are slower for the climate cooling scenarios. Regarding Q_{spr}, slower ground surface cooling flattens the curve so that the rates of change and peak Q_{spr} values are smaller. The greatest difference in peak Q_{spr} is observed between the minimum matrix compressibility cases with 0.47 L s^{-1} and 2.1 L s^{-1} for the climate cooling and exposure scenarios, respectively (Figure 4a).

4. Discussion and Conclusions

Our model was set up to simulate spring discharge generated solely by aggrading permafrost due to the pressure build-up from freezing expansion. As such, the ground surface temperature at the location of the spring was controlled by the temperature of the discharging groundwater rather than by the freezing temperature forced at the remaining model surface boundary. Lateral freezing could still occur in the model, and eventually led to closing of the taliks in our model scenarios. A smaller spring zone radius resulted in more rapid freezing of the spring talik and a shorter period with spring discharge. In reality, the thermal dynamics at the ground surface by a spring includes several processes that were excluded from the model—for example, the release of latent heat at the surface when spring water freezes to form an icing. The timing of spring freeze-up and its relation to spring zone radius should therefore be interpreted with caution. However, our model clearly shows that the active period for springs increases with greater catchment area, hydraulic conductivity, porosity, and matrix compressibility.

As the talik decreased in size with freezing, the simulated talik pore water velocity increased. The velocity peaked just when unfrozen ground (i.e., ground at $T > 0$°C) below the spring zone was gone and only partially or completely frozen ground remained. The peak in pore water velocity always occurred after peak spring discharge. During talik closure, increasing rates of advective heat transport, which are associated with the pore water velocity, will slow the closure and act as a buffer until ice starts to fill the pore space. Together with an expected increase of salinity due to solute-rejection (Panday & Corapcioglu, 1991), increasing advective heat transfer during initial talik closure functions as a negative feedback that may explain why even low-discharge permafrost springs can persist for relatively long periods. The decreasing groundwater travel-time through the talik during its closure could have a significant impact on solute transport—especially for reactive solutes. Brief travel-times may, for example, explain dissolved concentrations of methane exceeding the solubility limit in pingo spring water in Svalbard (Hodson et al., 2020).

Our modeling results suggest that hydraulic pressure generation from permafrost aggradation under optimal conditions can explain spring discharge of up to a couple of liters per second. For spring systems located in relatively young permafrost and with relatively low discharge rates (on the order of 0.1 L), such as typically found at open-system pingos in Svalbard (Demidov et al., 2019; Hornum et al., 2020, 2021; Liestøl, 1996; Matsuoka et al., 2004), hydraulic pressures generated by permafrost aggradation should be considered as the main driving mechanism—especially when obvious surface recharge sources are lacking. However, the pressure build-up underneath aggrading permafrost does not exclude other pressure sources, so—depending on the specific settings in a natural permafrost spring system, other mechanisms that generate groundwater flow should also be considered.

A unimodal appearance of discharge time curves was consistently simulated for all scenarios. Given this relatively simple pattern, field observations of spring discharge could, in principle, be used to deduce for example, the aquifer size, although other parameters need to be known with reasonable accuracy (as shown for permafrost catchments, Hinzman et al., 2022; Sergeant et al., 2023).

The world's permafrost regions are presently subject to thawing because of climate warming (Biskaborn et al., 2019). Permafrost-aggradation-related hydraulic head production may therefore seem irrelevant to present-day cold region hydrology. However, as we show here, there is a time lag between atmospheric temperature changes and its impacts on deep ground temperatures which implies that, in areas with relatively young permafrost (<10 ka), millennial-scale basal permafrost aggradation still takes place even when shallow permafrost is thawing (Hornum et al., 2020). Moreover, climate warming paradoxically also drives local development of permafrost when glacial retreat or regression of the sea due to uplift exposes previously unfrozen ground to cold air temperatures, such as after the Last Glacial Maximum (Vliet-Lanoë & Lisitsyna, 2001). In our simulations, permafrost aggradation generates pressure gradients to sustain artesian spring discharge over millennial

timescales after surface cooling has ceased. This is valid both in scenarios with slow and with rapid cooling, such as expected following exposure to terrestrial climate settings after the retreat of ice sheets or seas. This process for generating spring discharge is therefore likely still relevant in many of the current permafrost regions, especially those that were ice covered during the last glaciation. It is also relevant to consider for the long-term safety of hazardous materials, such as nuclear waste, as it provides a mechanism for contaminants to spread from the deep subsurface to surface systems.

Data Availability Statement

No new data was used in the creation of this manuscript. Model simulations were performed with FlexPDE version 7.19, a finite element builder and partial differential equations solver (PDE Solutions Inc., 2021). FlexPDE is freely available in a light version. Figures 1 and 2 were made with the open-source vector graphics editor Inkscape version 1.1 (Inkscape Developers, 2021) available under the GNU GPL license. Figures 3 and 4 were made with the computing environment MATLAB version 2022a (MathWorks®, 2022) and with Inkscape.

Acknowledgments
This work was conducted within the Catchment Transport and Cryohydrology Network (CatchNet) funded by the Swedish Nuclear Fuel and Waste Management Company (SKB). Lisse Verbakel was involved in the early stages of designing this study, and we would like to acknowledge her contribution. We thank one anonymous reviewer for providing thougtful review comments.

References

Andersen, D. T., Pollard, W. H., McKay, C. P., & Heldmann, J. (2002). Cold springs in permafrost on Earth and Mars. *Journal of Geophysical Research: Planets*, *107*(3), 1–7. https://doi.org/10.1029/2000je001436

Ballantyne, C. K. (2018). *Periglacial geomorphology*. John Wiley & Sons Ltd.

Bense, V. F., Ferguson, G., & Kooi, H. (2009). Evolution of shallow groundwater flow systems in areas of degrading permafrost. *Geophysical Research Letters*, *36*(22), L22401. https://doi.org/10.1029/2009GL039225

Biskaborn, B. K., Smith, S. L., Noetzli, J., Matthes, H., Vieira, G., Streletskiy, D. A., et al. (2019). Permafrost is warming at a global scale. *Nature Communications*, *10*(1), 1–11. https://doi.org/10.1038/s41467-018-08240-4

Briner, J. P., McKay, N. P., Axford, Y., Bennike, O., Bradley, R. S., de Vernal, A., et al. (2016). Holocene climate change in Arctic Canada and Greenland. *Quaternary Science Reviews*, *147*, 340–364. https://doi.org/10.1016/j.quascirev.2016.02.010

de Bruin, J. G. H., Bense, V. F., & van der Ploeg, M. J. (2021). Inferring permafrost active layer thermal properties from numerical model optimization. *Geophysical Research Letters*, *48*(16), 13. https://doi.org/10.1029/2021GL093306

Demidov, N., Wetterich, S., Verkulich, S., Ekaykin, A., Meyer, H., Anisimov, M., et al. (2019). Geochemical signatures of pingo ice and its origin in Grøndalen, west Spitsbergen. *The Cryosphere*, *13*(11), 3155–3169. https://doi.org/10.5194/tc-13-3155-2019

England, J. (1992). Postglacial emergence in the Canadian High Arctic: Integrating glacioisostasy, eustasy, and late deglaciation. *Canadian Journal of Earth Sciences*, *29*(5), 984–999. https://doi.org/10.1139/e92-082

Farouki, O. T. (1981). *Thermal properties of soils - CRREL monograph*. US Army Cold Regions Research and Engineering Laboratory.

French, H., & Shur, Y. (2010). The principles of cryostratigraphy. *Earth-Science Reviews*, *101*(3–4), 190–206. https://doi.org/10.1016/j.earscirev.2010.04.002

Garcia-Oteyza, J., Oliva, M., Palacios, D., Fernández-Fernández, J. M., Schimmelpfennig, I., Andrés, N., et al. (2022). Late Glacial deglaciation of the Zackenberg area, NE Greenland. *Geomorphology*, *401*, 108125. https://doi.org/10.1016/J.GEOMORPH.2022.108125

Grasby, S. E., Proemse, B. C., & Beauchamp, B. (2014). Deep groundwater circulation through the High Arctic cryosphere forms Mars-like gullies. *Geology*, *42*(8), 651–654. https://doi.org/10.1130/G35599.1

Grenier, C., Anbergen, H., Bense, V., Chanzy, Q., Coon, E., Collier, N., et al. (2018). Groundwater flow and heat transport for systems undergoing freeze-thaw: Intercomparison of numerical simulators for 2D test cases. *Advances in Water Resources*, *114*, 196–218. https://doi.org/10.1016/j.advwatres.2018.02.001

Grenier, C., Régnier, D., Mouche, E., Benabderrahmane, H., Costard, F., & Davy, P. (2013). Impact of permafrost development on groundwater flow patterns: A numerical study considering freezing cycles on a two-dimensional vertical cut through a generic river-plain system. *Hydrogeology Journal*, *21*(1), 257–270. https://doi.org/10.1007/s10040-012-0909-4

Guimond, J. A., Mohammed, A. A., Walvoord, M. A., Bense, V. F., & Kurylyk, B. L. (2021). Saltwater intrusion intensifies coastal permafrost thaw. *Geophysical Research Letters*, *48*(19), 1–10. https://doi.org/10.1029/2021GL094776

Guimond, J. A., Mohammed, A. A., Walvoord, M. A., Bense, V. F., & Kurylyk, B. L. (2022). Sea-level rise and warming mediate coastal groundwater discharge in the Arctic. *Environmental Research Letters*, *17*(4), 045027. https://doi.org/10.1088/1748-9326/AC6085

Haldorsen, S., Heim, M., & Lauritzen, S. E. (1996). Subpermafrost groundwater, western Svalbard. *Nordic Hydrology*, *27*(1–2), 57–68. https://doi.org/10.2166/nh.1996.0019

Hinzman, M. A., Sjöberg, Y., Lyon, S., Schaap, P., & van der Velde, Y. (2022). Using a mechanistic model to explain the rising non-linearity in storage discharge relationships as the extent of permafrost decreases in Arctic catchments. *Journal of Hydrology*, *612*, 13. https://doi.org/10.1016/j.jhydrol.2022.128162

Hodson, A., Nowak, A., Hornum, M. T., Senger, K., Redeker, K. R., Christiansen, H. H., et al. (2020). Sub-permafrost methane seepage from open-system pingos in Svalbard. *The Cryosphere*, *14*(11), 3829–3842. https://doi.org/10.5194/tc-14-3829-2020

Hornum, M. T., Betlem, P., & Hodson, A. (2021). Groundwater flow through continuous permafrost along geological boundary revealed by electrical resistivity tomography. *Geophysical Research Letters*, *48*(14), 1–11. https://doi.org/10.1029/2021GL092757

Hornum, M. T., Hodson, A., Jessen, S., Bense, V., & Senger, K. (2020). Numerical modelling of permafrost spring discharge and open-system pingo formation induced by basal permafrost aggradation. *The Cryosphere*, *14*(12), 4627–4651. https://doi.org/10.5194/tc-14-4627-2020

Humlum, O., Elberling, B., Hormes, A., Fjord, K., Hansen, O. H., & Heinemeier, J. (2005). Late-Holocene glacier growth in Svalbard, documented by subglacial relict vegetation and living soil microbes. *The Holocene*, *15*(3), 396–407. https://doi.org/10.1191/0959683605hl817rp

Ingólfsson, Ó., & Landvik, J. Y. (2013). The Svalbard-Barents Sea ice-sheet - Historical, current and future perspectives. *Quaternary Science Reviews*, *64*, 33–60. https://doi.org/10.1016/j.quascirev.2012.11.034

Inkscape Developers. (2021). Inkscape version 1.1. Retrieved from https://inkscape.org/release/inkscape-1.1/

Johansson, E., Gustafsson, L. G., Berglund, S., Lindborg, T., Selroos, J. O., Claesson Liljedahl, L., & Destouni, G. (2015). Data evaluation and numerical modeling of hydrological interactions between active layer, lake and talik in a permafrost catchment, Western Greenland. *Journal of Hydrology*, *527*, 688–703. https://doi.org/10.1016/j.jhydrol.2015.05.026

Kleinberg, R. L., & Griffin, D. D. (2005). NMR measurements of permafrost: Unfrozen water assay, pore-scale distribution of ice, and hydraulic permeability of sediments. *Cold Regions Science and Technology*, *42*(1), 63–77. https://doi.org/10.1016/j.coldregions.2004.12.002

Kooi, H. (1999). Competition between topography- and compaction-driven flow in a confined aquifer: Some analytical results. *Hydrogeology Journal*, *7*(3), 245–250. https://doi.org/10.1007/s100400050198

Kooi, H., Garavito, A. M., & Bader, S. (2003). Numerical modelling of chemical osmosis and ultrafiltrationacross clay formations. *Journal of Geochemical Exploration*, *78–79*, 333–336. https://doi.org/10.1016/S0375-6742(03)00038-4

Lamontagne-Hallé, P., McKenzie, J. M., Kurylyk, B. L., Molson, J., & Lyon, L. N. (2020). *Guidelines for cold-regions groundwater numerical modeling* (pp. 1–26). Wiley Interdisciplinary Reviews: Water. https://doi.org/10.1002/wat2.1467

Liestøl, O. (1977). Pingos, springs, and permafrost in Spitsbergen. In A. Brekke (Ed.), *Norsk Polarinstitutt Årbok 1975* (pp. 7–29). Universitetsforlaget.

Liestøl, O. (1996). Open-system pingos in Spitsbergen. *Norsk Geografisk Tidsskrift*, *50*(1), 81–84. https://doi.org/10.1080/00291959608552355

Lindgren, A., Hugelius, G., Kuhry, P., Christensen, T. R., & Vandenberghe, J. (2016). GIS-based maps and area estimates of Northern Hemisphere permafrost extent during the Last Glacial Maximum. *Permafrost and Periglacial Processes*, *27*(1), 6–16. https://doi.org/10.1002/ppp.1851

Mackay, J. R. (1998). Pingo growth and collapse, Tuktoyaktuk Peninsula area, western arctic coast, Canada: A long-term field study. *Géographie Physique et Quaternaire*, *52*(3), 271–323. https://doi.org/10.7202/004847ar

Mangerud, J., & Svendsen, J. I. (2017). The Holocene thermal maximum around Svalbard, Arctic North Atlantic; molluscs show early and exceptional warmth. *The Holocene*, *28*(1), 65–83. https://doi.org/10.1177/0959683617715701

MathWorks® (2022). MATLAB R2022a. Retrieved from https://se.mathworks.com/products/matlab.html

Matsuoka, N., Sawaguchi, S. I., & Yoshikawa, K. (2004). Present-day periglacial environments in Central Spitsbergen, Svalbard. *Geographical Review of Japan*, *77*(6), 276–300. https://doi.org/10.4157/grj.77.276

McKenzie, J. M., Voss, C. I., & Siegel, D. I. (2007). Groundwater flow with energy transport and water-ice phase change: Numerical simulations, benchmarks, and application to freezing in peat bogs. *Advances in Water Resources*, *30*(4), 966–983. https://doi.org/10.1016/j.advwatres.2006.08.008

Mohammed, A. A., Bense, V. F., Kurylyk, B. L., Jamieson, R. C., Johnston, L. H., & Jackson, A. J. (2021). Modeling reactive solute transport in permafrost-affected groundwater systems. *Water Resources Research*, *57*(7), 1–20. https://doi.org/10.1029/2020WR028771

Mohammed, A. A., Guimond, J., Bense, V., Jamieson, R., McKenzie, J. M., & Kurylyk, B. (2022). Mobilization of subsurface carbon pools driven by permafrost thaw and reactivation of groundwater flow: A virtual experiment. *Environmental Research Letters*, *17*(12), 124036. https://doi.org/10.1088/1748-9326/ACA701

Mottaghy, D., & Rath, V. (2006). Latent heat effects in subsurface heat transport modelling and their impact on palaeotemperature reconstructions. *Geophysical Journal International*, *164*(1), 236–245. https://doi.org/10.1111/j.1365-246X.2005.02843.x

Neuzil, C. E. (1995). Abnormal pressures as hydrodynamic phenomena. *American Journal of Science*, *295*(6), 742–786. https://doi.org/10.2475/ajs.295.6.742

Panday, S., & Corapcioglu, M. Y. (1991). Solute rejection in freezing soils. *Water Resources Research*, *27*(1), 99–108. 90WR0178. https://doi.org/10.1029/90wr01785

PDE Solutions Inc. (2021). FlexPDE version 7.19. Retrieved from https://www.pdesolutions.com/sdmenu7.html

Pirazzoli, P. A., & Pluet, J. (1991). World atlas of Holocene sea-level changes. In *Elsevier oceanography series* (1st ed., Vol. 58). Elsevier. Retrieved from http://www.sciencedirect.com/science/article/pii/S0422989408705920

Saito, K., Okuno, J., Machiya, H., Iwahana, G., Ohno, H., & Yokohata, T. (2022). Climatic assessment of circum-Arctic permafrost zonation over the last 122 kyr. *Polar Science*, *31*, 100765. https://doi.org/10.1016/j.polar.2021.100765

Scheidegger, J. M., & Bense, V. F. (2014). Impacts of glacially recharged groundwater flow systems on talik evolution. *Journal of Geophysical Research: Earth Surface*, *119*(4), 758–778. https://doi.org/10.1002/2013JF002894

Scheidegger, J. M., Bense, V. F., & Grasby, S. E. (2012). Transient nature of Arctic spring systems driven by subglacial meltwater. *Geophysical Research Letters*, *39*(12), 1–6. https://doi.org/10.1029/2012GL051445

Scholz, V. H., & Grottenthaler, W. (1988). Beiträge zur jungholozänen Deglaziationsgeschichte im mittleren Westgrönland. *Polarforschung*, *58*(1), 25–40. https://doi.org/10.2312/polarforschung.58.1.25

Sergeant, F., Therrien, R., Anctil, F., & Gatel, L. (2023). Simulating the recession dynamics of Arctic catchments in the context of a thawing permafrost. *Journal of Hydrology*, *623*, 13. https://doi.org/10.1016/j.jhydrol.2023.129847

Sjöberg, Y., Marklund, P., Pettersson, R., & Lyon, S. W. (2015). Geophysical mapping of palsa peatland permafrost. *The Cryosphere*, *9*(2), 465–478. https://doi.org/10.5194/tc-9-465-2015

Tóth, J. (1970). A conceptual model of the groundwater regime and the hydrogeologic environment. *Journal of Hydrology*, *10*(2), 164–176. https://doi.org/10.1016/0022-1694(70)90186-1

Vliet-Lanoë, B., & Lisitsyna, O. (2001). Permafrost extent at the Last Glacial Maximum and at the Holocene optimum. The climex map. In R. Paepe, V. Melnikov, E. Overloop, & V. D. Gorokhov (Eds.), *Permafrost response on economic development, environmental security and natural resources* (pp. 215–225). Kluwer Academic Publishers. https://doi.org/10.1007/978-94-010-0684-2_14